

Mechanistic insights in phosphorene degradation

Rohit Babar¹ and Mukul Kabir^{1,2,*}

¹*Department of Physics, Indian Institute of Science Education and Research, Pune 411008, India*

²*Centre for Energy Science, Indian Institute of Science Education and Research, Pune 411008, India*



(Received 30 May 2019; published 29 July 2019)

The structural and chemical degradations of phosphorene severely limit its practical applications despite the enormous promise. In this regard, we investigate a cohort of microscopic kinetic mechanisms and develop a degradation phase diagram using first-principles calculations. At 400 K, the degradation and the competing self-annealing proceeds through the merger and annihilation of vacancies, which are triggered via itinerant vacancies and adatoms. A further increase in temperature beyond 650 K, the structural degradation results through the emission of the undercoordinated atoms from the defect and the concurrent pairwise sublimation. The role of interlayer vacancy diffusion is discarded in the context of structural degradation. The chemical degradation proceeds through the dissociation of an oxygen molecule that is activated at the room temperature on the pristine surface or spontaneous at the single-vacancy site. The present results are in agreement with the few available experimental conjectures and will motivate further efforts.

DOI: [10.1103/PhysRevMaterials.3.074008](https://doi.org/10.1103/PhysRevMaterials.3.074008)

I. INTRODUCTION

Few-layered black phosphorus (BP) has earned significant attention due to a layer-tuneable band gap between 0.2–2.2 eV and anisotropic mechanical, electronic and optical responses [1–8]. The staggered hexagonal layers of BP are stacked together by van der Waals interaction, similar to graphite. The isolated layers of BP, phosphorene, offers significant advantages in realizing novel semiconducting and optoelectronic devices due to its high current on-off ratio, extraordinary carrier mobility, ambipolar transport, and anisotropic electronic dispersion [1,2,8–11]. Moreover, the high mechanical flexibility and the retention of extraordinary electronic and optical properties under moderate strain allow to design functional heterostructures with other two-dimensional materials [7,12–14]. Further, many exotic quantum many-body states have been theoretically predicted and experimentally demonstrated in the few-layer phosphorene [15–17].

However, the major impediment is the inferior stability of phosphorene at ambient conditions compared to the graphene and transition-metal dichalcogenides. The degradation in two-dimension results from the dynamics of lattice defects and chemical interaction with the environment [18–21]. Both surface and subsurface defects have been experimentally observed in the few-layer phosphorene due to their low formation energies, which are responsible for intrinsic *p*-type conductivity [1,22–24]. Similar to graphene, the vacancy defects in phosphorene relaxes in multiple configurations [25,26], and act as anisotropic scatterers. Point defects have been further manipulated to produce a many-body state with excited carriers [22,27]. In addition to the disruption in the electronic properties, the vacancies in phosphorene induce mechanical degradation and produce structural changes un-

der increasing strain, temperature, or vacancy concentration [28–30]. Vacancy containing strained phosphorene reduces the fracture strength and structural integrity along the zigzag axis due to bond distortion and breakage. Further, regions with high defect density are predicted to initiate crack formation followed by the structural failure under the transverse force generated by an atomic force microscopy nanoindentation [31].

Thermally activated diffusion of point defects holds the key to the degradation in crystalline solids. Vacancy transformation, diffusion, and aggregation leading to the formation of complex defects and grain boundaries have been extensively studied in graphene [32,33], where the weak bonding at the edges and vacancies initiate structural degradations. The few-layer phosphorene is observed to undergo anisotropic degradation, amorphization, and sublimation at temperatures above 650 K [28,34,35]. However, the current description of structural degradation is limited to the diffusion of isolated vacancy within a single layer [26,36,37], which severely limits our microscopic understanding. In this regard, here we investigate a cohort of mechanisms involving vacancy and adatom migration, complex defect-defect interaction, and surficial desorption leading to the larger defect formation. The competing self-healing mechanisms of defects are also investigated. Such a comprehensive understanding of degradation, which will be presented here, is necessary to identify the optimal experimental conditions to prepare and restore the defect-free phosphorene.

The rapid oxidation of phosphorene in the ambient environment presents another significant challenge towards its stability. Although the exact mechanism continues to be investigated, it is understood that the strong chemical bonding between lone pair electrons of phosphorus and π^* electrons of oxygen initiate the chemical degradation [38–47]. Further, degradation is accelerated as the hydrophilicity of phosphorene increases with oxidation [38,41,47]. Moreover, the edges

*Corresponding author: mukul.kabir@iiserpune.ac.in

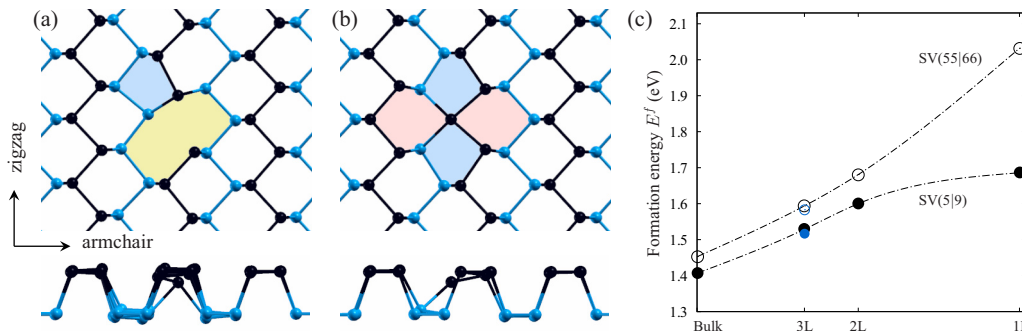


FIG. 1. The top and side views of the single-vacancy in phosphorene in its two possible configurations (a) SV(5|9) and (b) SV(55|66). Atoms in the two half-layers are coloured in blue and black. The polygons in the vacancy are shaded with different colours. (c) Formation energies E^f of the SV(5|9) and SV(55|66) defects at the apical layer with varied layer thickness. The E^f for the subsurface vacancy (blue circles) and bulk are also shown. The formation energy decreases with increasing layer thickness. While in single layer, the SV(5|9) is thermodynamically favourable over the SV(55|66) configuration by 350 meV, and the difference in energy between the defects also decreases with the thickness to 45 meV for the bulk black phosphorus. Note that the vacancy formation is much easier in the few-layer phosphorene owing to the much lower E^f compared to graphene and other mono-elemental bulk semiconductors [33,55,56].

and steps undergo rapid degradation in few-layered samples, where the role of vacancy defects is understandably negligible [42,44]. It is also observed that the oxidation rate increases with the reduction in the number of layers [39,43], which indicates a stronger interaction of oxygen at the surface.

However, the nature of oxygen-defect interaction in phosphorene is a subject of debate at present in the absence of experimental studies. While the oxidation is proposed to be an activated process, it is more favourable at a lattice vacancy than the pristine surface [48]. On the contrary, a weak interaction was suggested as the vacancy diffusion is found to be unaffected by oxygen [26]. In the present study, we thoroughly investigate the interaction of O_2 on the pristine and defected phosphorene. Further, the microscopic dissociation mechanism is illustrated. We find the O_2 dissociation to be a barrier-less process at the single vacancy defect, whereas oxidation on both pristine surface and at the divacancy defect remains an activated process. Once the dissociation is complete, the strong P-O binding essentially makes O removal from the lattice impossible.

II. COMPUTATIONAL DETAILS

The spin-polarized density functional theory calculations are performed within the projector augmented wave formalism [49], as implemented in the Vienna *ab initio* simulation package (VASP) [50,51]. The wave functions are described in the plane wave basis with 500 eV cutoff for the kinetic energy, and the exchange-correlation energy is expressed with the Perdew-Burke-Ernzerhof (PBE) functional [52]. Structural relaxations are performed until all the force components fall below 0.01 eV/Å threshold. Calculations on the single-layer phosphorene (SLP) are performed using two supercells with different sizes, 6 (zigzag) \times 4 (armchair) supercell containing 96 atoms and 9 (zigzag) \times 5 (armchair) supercell containing 180 atoms. The reciprocal space integration for the two supercells was evaluated with 4 \times 4 \times 1 and 3 \times 4 \times 1 k -point grids, respectively. A vacuum of 15 Å was always maintained perpendicular to the surface to minimize the spurious interaction between the periodic images. Calculations for the

few-layer phosphorene are performed using the 6 \times 4 \times N supercells ($N \leq 3$). The nonlocal van der Waals functional (optB88-vdW) of Langreth and Lundqvist is used throughout the calculations to describe the oxygen-phosphorene and interlayer interactions [53]. The activation barriers are calculated within the climbing image nudged elastic band method formalism [54]. The true nature of the transition states is confirmed by obtaining the single imaginary vibrational mode.

III. RESULTS AND DISCUSSION

The two half-layers in the hexagonal staggered lattice of SLP are separated by 2.13 Å (Fig. 1). The in-plane atoms are arranged in a zigzag fashion with 2.23 Å bonds (zigzag axis), whereas the atoms across the two half-layers have slightly larger bond lengths of 2.27 Å (armchair axis). Thus every P atom is bonded with two in-plane and one out-of-plane atoms. Given that each P atom has five valence electrons, three electrons participate in bonding, whereas rest of the electrons produce a lone-pair charge cloud. The Coulomb repulsion among the lone pairs leads to a staggered, anisotropic arrangement of P atoms with comparatively soft bonding (Fig. 1). Thus the Young's modulus for phosphorene is substantially lower than graphene [57,58].

Before we discuss the kinetics of point defects, we investigate the formation of lattice vacancy in the light of recent experimental observations. The removal of a single P atom introduces dangling electrons on the undercoordinated atoms, which concurrently undergo differential structural rearrangements to form two distinct defect configurations, SV(5|9) and SV(55|66) [Figs. 1(a) and 1(b)]. The SV(5|9) configuration results from the inward displacement of two atoms along the armchair direction to form a new P-P bond between the two half-layers, while the third P atom remains undercoordinated [Fig. 1(a)]. In comparison, the vacancy relaxation in graphene results in multiple Jahn-Teller distorted configurations, where the planar (5|9) vacancy is the ground state [33]. The second configuration SV(55|66) in phosphorene is generated through a minor displacement of atoms to form pentagon and hexagon pairs [Fig. 1(b)]. The P-P bond along the armchair direction

TABLE I. Formation energies E^f of the various defect complexes in SLP. The E^f is calculated as $E^f = E_{\text{tot}} - N_{\text{P}} \times E_{\text{P}}$, where E_{tot} is the total binding energy of the defect-containing supercell, and E_{P} is the binding energy per P atom in the pristine SLP. N_{P} is the number of P atoms in the defected lattice. The activation energies E_a , for the cohort of microscopic processes leading to the self-healing, degradation, and sublimation are calculated. Note that both vacancy and P-adatom P_{A} are highly itinerant due to lower E_a and the corresponding diffusion are highly anisotropic along the zigzag and armchair directions.

Defect complex	Formation energy E^f (eV)	Microscopic process	Activation barrier E_a (eV)
SV(5 9)	1.68	SV(5 9) \rightarrow SV(5 9)	0.12 (zigzag), 0.38 (armchair)
SV(55 66)	2.03	—	—
DV(5 8 5)	1.56	DV(5 8 5) \rightarrow SV(5 9) + SV(9 5)	1.64
SV(5 9) + SV(9 5)	2.52	SV(5 9) + SV(9 5) \rightarrow DV(5 8 5)	0.68
Single P_{A}	1.43	$P_{\text{A}} \rightarrow P_{\text{A}}$ P_{A} desorption	0.19 (zigzag), 1.05 (armchair) 2.14
P_{A} -pair	2.01	P_{A} -pair desorption	barrierless
SV(5 9) + P_{I}	1.56	SV(5 9) + $P_{\text{I}} \rightarrow$ pristine SLP pristine SLP \rightarrow SV(5 9) + P_{I}	0.69 2.25
SV(55 66) + P_{I}	1.93	SV(55 66) + $P_{\text{I}} \rightarrow$ SV(5 9) + P_{I}	0.07
DV(5 8 5) + P_{A}	2.68	DV(5 8 5) + $P_{\text{A}} \rightarrow$ SV(5 9) SV(5 9) \rightarrow DV(5 8 5) + P_{A}	0.46 1.46

(2.57 Å) at the SV(55|66) defect is weaker than both pristine (2.27 Å) and SV(5|9) defect with 2.41 Å bonds. Such fourfold coordination [Fig. 1(b)] also appears in rippled graphene due to increased sp^3 character [59].

The SV(5|9) vacancy is thermodynamically more stable than the SV(55|66) configuration [Fig. 1(c) and Table I]. Further, owing to a much lower E^f , the vacancy formation is significantly easier in phosphorene than in graphene (~ 7.5 eV) [33] and other mono-elemental bulk semiconductors such as Si and Ge ($E^f = 3.0\text{--}4.5$ eV) [55,56]. This indicates phosphorene to be defect-prone, and thus, the point-defect driven structural degradation becomes relevant. Further, the vacancy formation energy at the surface of a few-layer phosphorene decreases with the increasing layer thickness [Fig. 1(c)]. While the relative stability of SV(5|9) and SV(55|66) differs by 350 meV in a single layer, it decreases to 65 meV in 3L. Similarly, the calculated E^f for the subsurface SV(5|9) and SV(55|66) defects in 3L phosphorene is much lower, 1.54 and 1.60 eV, respectively, compared to the SLP (Table I).

A. Anisotropic vacancy migration

A complete understanding of migration mechanisms of a lattice vacancy in phosphorene becomes critical due to their significant presence owing to their low formation energies, and as they drive mechanical degradation [23]. Here, we investigate both intra- and interlayer vacancy diffusion and consider jumps along both the armchair and zigzag directions to understand the effects of structural anisotropy. Relating the various degradation mechanisms with the vacancy migration and the adatom mediated self-healing may assist in constructing a suitable defect annealing strategy.

The SV(5|9) migration in the SLP is directionally anisotropic, with substantially different barriers along the armchair and zigzag directions, 0.38 and 0.12 eV, respectively [Table I and Figs. 2(a) and 2(b)]. Along the armchair direction, the vacancy jump occurs via switching of bonds—the P atom of the pentagonal bond is displaced along the armchair

direction and subsequently bonds with the undercoordinated atom [Fig. 2(a)]. The undercoordinated atom then migrates to the bottom half-layer in the final configuration. The vacancy migration along the zigzag direction occurs analogously shown in Fig. 2(b); however, the migration is facile due to a much lower activation barrier. These results are in good agreement with the previously reported values of 0.18–0.40 eV [26,36,37].

In addition to the anisotropic migration, the vacancy jump mechanism discussed so far is uncommon, since the undercoordinated atom plays a minor role. Conventionally, the undercoordinated atom can detach easily and jump to the vacant lattice site. However, during the SV(5|9) vacancy migration, phosphorene retains the staggered arrangement by the switching of P–P bonds across the half-layers, which lowers the activation barrier. The overall diffusion occurs through a combination of anisotropic vacancy jumps and the diffusion along the armchair direction is the rate-limiting step with 0.38 eV barrier [Table I and Fig. 2(a)]. In contrast, a relatively high barrier of 0.72 eV was calculated for the vacancy migration in graphene [33]. The aggregation of vacancy defects in an anisotropic environment will lead to the formation of line defects and grain boundaries, which in turn will act as a sink for diffusing vacancies [37].

Now, we investigate the effect of layer thickness on the in-plane vacancy diffusion, and also discuss how the migration is affected while the vacancy is embedded in the few-layer phosphorene (Fig. 3). In 2L phosphorene, the activation barrier decreases to 0.28 and 0.07 eV, respectively, for diffusion along the armchair and zigzag directions (Fig. 3). We do not anticipate a further reduction in E_a with increasing thickness. While the mechanism remains the same, the subsurface vacancy diffusion is easier as revealed by the lower activation barrier (Fig. 3). For subsurface SV(5|9) migration in 3L phosphorene, the calculated E_a are found to be 0.22 and 0.04 eV along the armchair and zigzag directions, respectively. Therefore, in 3L phosphorene, the E_a for the subsurface diffusion converges to the bulk BP, which we find to be 0.2 and 0.04 eV,

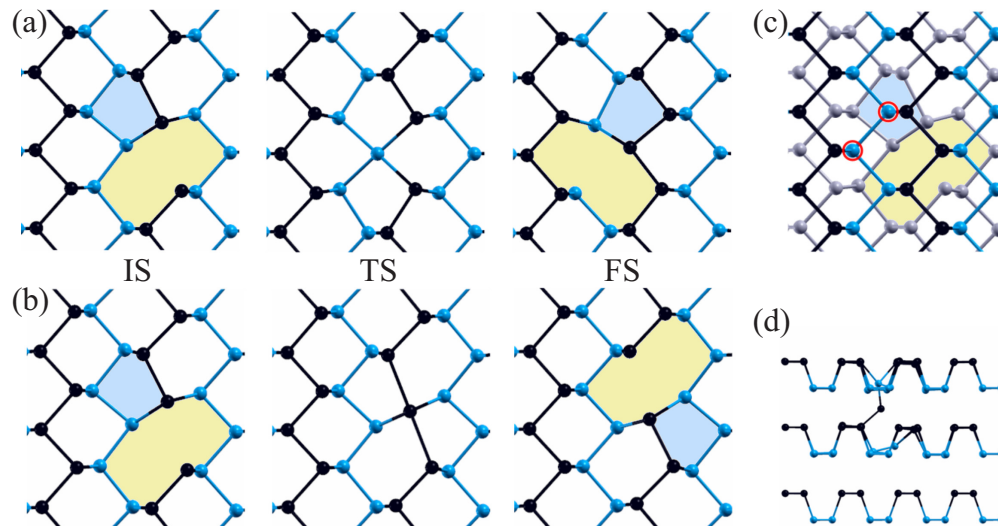


FIG. 2. The intralayer SV(5|9) migration mechanisms along the (a) armchair and (b) zigzag crystallographic directions. The respective initial state (IS), transition state (TS) and final state (FS) are shown. The TS configurations are markedly different from each other, which leads to distinct activation barriers along the armchair and zigzag directions (Table I). (c) The interlayer SV(5|9) migration is studied by considering two different pathways, where either of the nearest and next-nearest-neighbor atoms from the undefected half-layer jumps to the defected layer. The migrating atoms are encircled in red color, and the grey atoms belong to the defected layer. (d) The side view showing the interlayer P-P bonding for the corresponding transition state.

respectively (Fig. 3). These results are in contrast to the few-layer graphene and graphite, where the activation barrier is higher for the subsurface vacancy diffusion [33,60,61], and the microscopic origin has been discovered only recently [33]. In single-layer graphene, the strain generated in the lattice due to the vacancy diffusion is released by an out-of-plane buckling, whereas the lattice relaxation within the half-layers releases the corresponding strain in phosphorene. As the

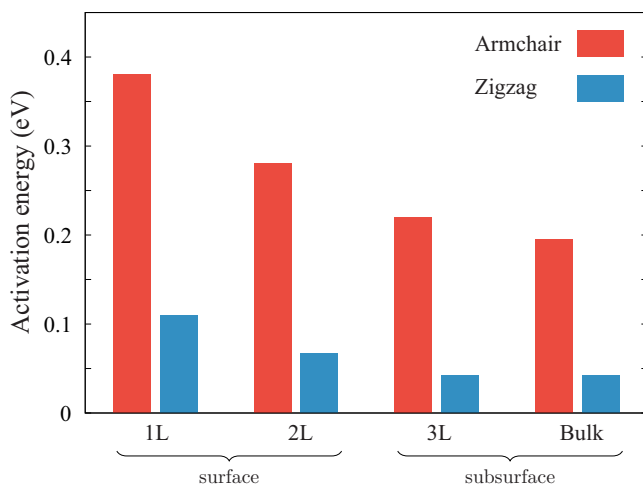


FIG. 3. Activation barriers for the in-plane diffusion of SV(5|9) vacancy at the surface and subsurface. The anisotropic crystal structure of phosphorene results in two distinct migration pathways along the armchair and zigzag directions with different activation barriers. Calculated barriers for the surface vacancy depend on the layer thickness. Further, the barriers are much smaller for the subsurface migration compared to the vacancy at the surface.

out-of-plane buckling is restricted in multi-layered graphene, the E_a for the surface and subsurface vacancy increases substantially in few-layer graphene. In contrast, the lower E_a in few-layer phosphorene is due to the reduction in the corresponding formation energies as discussed earlier [Fig. 1(c)] [24,62]. A similar Brønsted-Evans-Polanyi-type correlation between E^f and E_a has been reported in other bulk semiconductors and carbon nanotubes [63–65].

With a lower E^f at the subsurface, it would be interesting to investigate the subsurface SV(5|9) vacancy diffusion to the surface. Due to the AB stacking in few-layer phosphorene, the vacancies in adjacent layers do not align vertically and thus diffuses via interlayer diagonal jumps [Fig. 2(c)]. We considered the two possible pathways, where either of the nearest- and next-nearest-neighbor atom from the adjacent undefective layer migrates to the SV(5|9) vacancy. In both mechanisms, the migrating P-atom bonds with both active layers [Fig. 2(d)] and resembles with the Wigner defect [66]. While the interlayer SV(5|9) migration via the nearest P-atom jump is calculated to be 2.17 eV, the second mechanism costs much higher activation energy of 2.80 eV. Such substantial interlayer barrier restricts the vacancy migration across the layers to very high temperature and will not play any significant role in the annealing process, which is usually performed at temperatures around 475 K [28]. In comparison, the corresponding barrier is significantly higher in the few-layer graphene, 5.5–7.0 eV, and becomes relevant only above 2000 K [67,68]. However, in the presence of complex defect structures, the interlayer vacancy migration may occur at a much lower temperature. The similar increase in interlayer activity is reported in the few-layer phosphorene above 600 K, while such interlayer defect complexes are present [34].

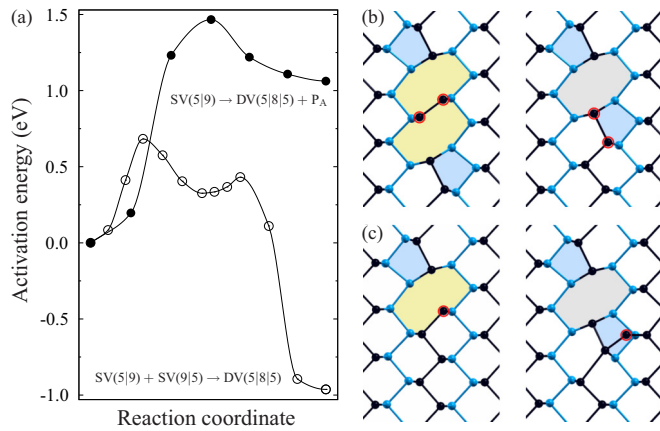


FIG. 4. (a) The energy profiles for the mechanisms leading to the larger defect formation, $SV(5|9) + SV(9|5) \rightarrow DV(5|8|5)$ and $SV(5|9) \rightarrow DV(5|8|5) + P_A$. Owing to a lower 0.68 eV barrier, $DV(5|8|5)$ is generated via coalescence of itinerant $SV(5|9)$ vacancies. While the forward $SV(5|9) \rightarrow DV(5|8|5) + P_A$ process has a high barrier, note that the reverse self-healing process has a much lower barrier of 0.46 eV. [(b) and (c)] The corresponding initial and final structures. (b) The merger of mono-vacancies into $DV(5|8|5)$ through bond rotation (encircled in red). (c) The structures for the $SV(5|9) \rightarrow DV(5|8|5) + P_A$ mechanism.

B. Vacancy-driven degradation, void formation, and sublimation

Recent experiments indicate that heating of few-layer phosphorene creates oblate voids in the individual layers, which is followed by the interlayer P–P bond formation. Further, the degradation proceeds via amorphization and eventual sublimation between 650–680 K [28,34,35]. Thus, to achieve a better understanding of structural degradation, we investigate a cohort of mechanisms such as self-healing, $[SV + SV] \rightarrow DV$ (divacancy), $SV \rightarrow [DV + P_A]$ pair transformations, and sublimation (Table I).

The divacancy defect $DV(5|8|5)$ is formed by the removal of two adjacent P atoms from the same half-layer. The concurrent structural relaxation to pentagon-octagon-pentagon arrangement ensures threefold coordination for all the atoms with a formation energy of 1.56 eV, which is lower than the $SV(5|9)$ defect formation. Although the $DV(5|8|5)$ has not been yet observed in the low-temperature experiments below 10 K [22,23], it should be formed during exfoliation or by the coalescence of two itinerant $SV(5|9)$ defects. Further, the $[SV(5|9) + SV(9|5)] \rightarrow DV(5|8|5)$ merger (Ref. [69]) is viewed as one of the relevant mechanisms for multivacancy defect formation, and the calculated barrier is found to be 0.68 eV [Table I and Fig. 4(a)]. The corresponding mechanism is shown in the Fig. 4(b). The reverse mechanism of $DV(5|8|5)$ splitting into two adjacent vacancies requires much higher energy of 1.64 eV. Thus the itinerant SV defects will easily coalesce to form $DV(5|8|5)$ and larger defects. In contrast to the present calculations, a much smaller barrier of 1.05 was estimated earlier for the $DV(5|8|5) \rightarrow [SV(5|9) + SV(9|5)]$ dissociation. [26] The discrepancy arises since the previous estimate is based on the energy differences between the DV and $[SV + SV]$ structures only and without the kinetic

consideration of bond reorientation. The split vacancy may also diffuse away, along the armchair and zigzag directions, with activation barriers that decrease with increasing separation. The calculated E_a converges to the isolated vacancy migration, while the vacancies are sufficiently separated [69]. While compared with the single-layer graphene, the DV defects are known to be stable due to a much high barrier for dissociation above 5 eV [70,71].

At present, the proposed mechanism, for the anisotropic void formation that is experimentally observed above 650 K, is the removal of edge atoms from the defects [28,34,35]. However, the corresponding rate-determining atomistic process is not yet known. In this regard, we investigate the transformation of an $SV(5|9)$ into the $[DV(5|8|5) + P_A]$ complex, where the undercoordinated P atom of the $SV(5|9)$ migrates to the nearest bridge site [Fig. 4(c)]. An activation barrier of 1.46 eV is calculated for this mechanism [Table I and Fig. 4(c)], which is in excellent agreement with the experimental estimate of 1.64 ± 0.1 eV [35]. Subsequent removal of the peripheral atoms will require a similar or lower barrier due to weak bonding at the edges and will result in void formation. Further, the P_A adatoms generated in the above process will diffuse along the zigzag direction with remarkably low migration barrier of 0.19 eV, which is much higher 1.05 eV along the armchair direction (Table I).

As the temperature is further increased above 625 K, the degradation process is accelerated, and results in rapid sublimation between 650–680 K [28,34,35]. We address the sublimation process by considering the desorption of single and paired P adatoms that are produced during the $SV(5|9) \rightarrow [DV(5|8|5) + P_A]$ process. The single P_A on the pristine surface binds at the bridge site connecting the two armchair edges with 1.43 eV formation energy. The shorter adatom-surface separation of 2.19 Å highlights the role of lone-pair electrons in the bonding. The desorption mechanism is modelled by vertically detaching the P_A by 6 Å from the surface, which requires overcoming a minimum barrier of 2.14 eV (Table I).

Highly itinerant P_A on the surface forms P_A pairs, and we investigate the simultaneous desorption of both P adatoms. Two adjacent P_A (Ref. [69]) along the zigzag directions is found to be thermodynamically most favourable with 2.01 eV formation energy. Thus, the pair formation is thermodynamically advantageous than the two noninteracting P_A s, which favours aggregation of adatoms. Further, the desorption of P_A pair is found to be a spontaneous process without an activation barrier, and the free-energy is reduced by 0.82 eV/ P_A pair. Therefore we conclude that the itinerant P_A s thermodynamically form P_A pairs, and its concurrent desorption is critical to the rapid sublimation of phosphorene. These results are in excellent agreement with the recent experimental hypothesis of pairwise sublimation [35].

We argue that the origin of anisotropic void formation is twofold—directional anisotropy in both vacancy and adatom diffusion. Faster vacancy diffusion along the zigzag direction triggers multivacancy defects that are elongated along the zigzag direction. Further, the faster adatom diffusion along the zigzag path produces P_A pairs promoting sublimation. Thus these processes will create anisotropic voids with the long axis along the zigzag direction, which is in agreement with the recent experimental observations [35,72].

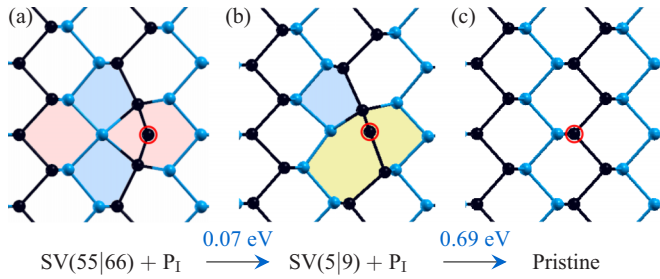


FIG. 5. Self-healing mechanisms of a vacancy via the recombination with P interstitial P₁ (encircled by red color), which are rate-limited by 0.69 eV activation barrier (Table I). Frenkel defects (a) SV(55|66) + P₁ and (b) SV(5|9) + P₁ recombine to form pristine lattice in (c). The numbers in blue color indicate the corresponding activation barrier. The interstitial P₁ in the Frenkel defects preferentially binds along the zigzag direction, and these complexes are thermodynamically stable at room temperature. Meanwhile, the DV(5|8|5) is partially healed first to an SV(5|9) defect by absorbing an itinerant P_A adatom, which requires 0.46 eV energy (Table I and Fig. 4).

C. Defect healing and the role of P adatom

Point defects can generate larger defects via various mechanisms that are discussed above. However, the point defects can also be self-healed by the interaction with the adatoms or interstitial defects, which we investigate in detail. The vacancy-interstitial (P₁) Frenkel pairs with SV(5|9) and SV(55|66) vacancies [Figs. 5(a) and 5(b)] are stable with 1.56 and 1.93 eV formation energies, respectively. In comparison, such Frenkel defects are absent in graphene due to the dominant nature of strong sp² bonding, which prevents out-of-plane geometry of the C adatom within the graphene vacancy. The self-healing of SV(5|9) by interstitial P₁ [Fig. 5(b) \rightarrow 5(c)] requires a moderate E_a of 0.69 eV. In contrast, the relatively less stable SV(55|66) and interstitial pair [Fig. 5(a)] first converts into an intermediate [SV(5|9) + P₁] pair [Fig. 5(b)] with 0.07 eV activation energy (Table I). In contrast, the reverse mechanism of [SV(5|9) + P₁] Frenkel pair generation at the pristine lattice requires substantially higher energy of 2.25 eV (Table I).

Having studied the self-healing of single vacancy, we now investigate the DV(5|8|5) healing. The partial healing of DV(5|8|5) to SV(5|9) by an itinerant P_A requires an activation barrier of 0.46 eV [Table I and Fig. 4(c)], and this process is accessible at 300 K [Figs. 5(d) and 5(e)]. The complete healing of DV then proceeds via the absorption of another mobile P_A into the SV with 0.69-eV barrier as discussed earlier, which is the rate-limiting process and occurs at a higher temperature above 450 K [28]. In contrast to phosphorene, this process requires 0.9 eV of energy in graphene and thus, the adatom-DV(5|8|5) complex is experimentally observed at room temperature [71,73,74].

D. Oxidation of pristine and defected phosphorene

In addition to the defect-mediated structural degradation, phosphorene also undergoes chemical degradation in the ambient environment. In this regard, we investigate the O₂-dissociation mechanism on the pristine and defected

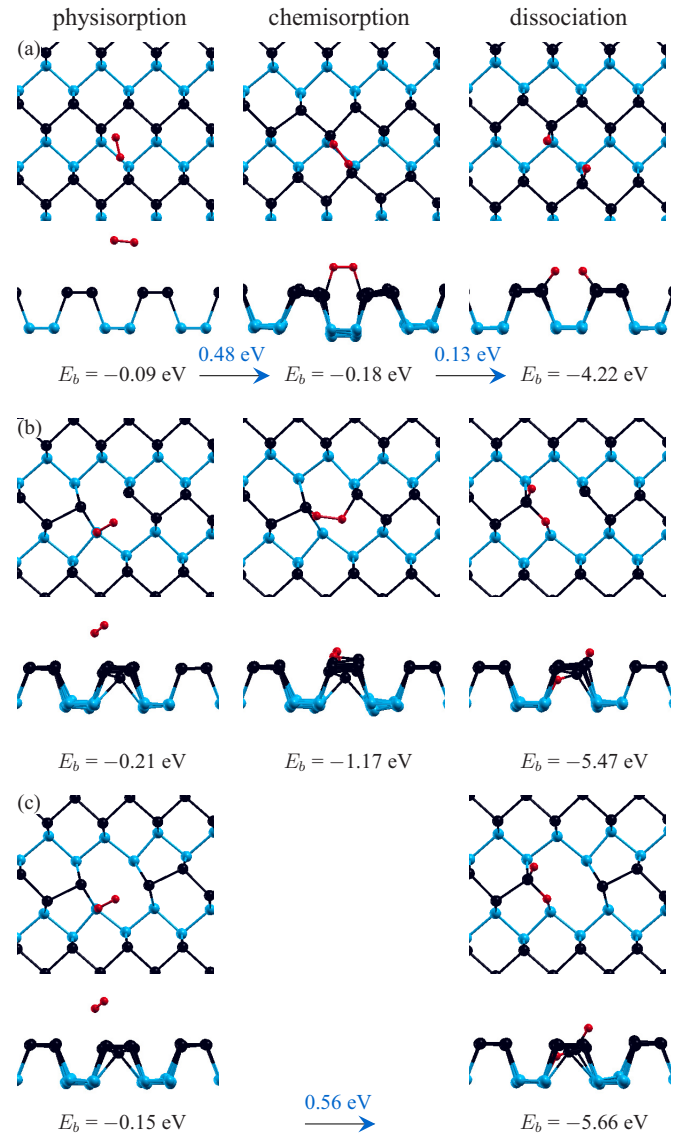


FIG. 6. The chemical degradation of phosphorene through oxidation. The top and side views for O₂ dissociation are shown (a) on the pristine surface; and at the (b) SV(5|9) and (c) DV(5|8|5) defect sites. While the entire physisorption \rightarrow chemisorption \rightarrow dissociation process is activated on the pristine surface with 0.48 eV rate-limiting barrier, the same is spontaneous at the SV(5|9) vacancy. We did not find any chemisorbed configuration at the DV(5|8|5) defect, and the O₂ dissociation directly proceeds from the physisorbed structure with 0.56-eV barrier. For all cases, the dissociated O atoms bind strongly with the phosphorene, and would thus be impossible to remove from the lattice. The numbers in blue color indicate the corresponding activation barrier.

phosphorene [69]. The binding energy is calculated as $E_b = E_{(\text{SLP}-\text{O}_2)} - E_{\text{SLP}} - E_{\text{O}_2}$, where E_{SLP} is the energy of the pristine SLP, E_{O_2} is the energy of the O₂ molecule and $E_{(\text{SLP}-\text{O}_2)}$ is the energy of the interacting composite system. The physisorbed O₂ molecule is very weakly bound ($E_b = -0.09 \text{ eV}$) to the SLP at 3.17 Å vertical height [Fig. 6(a)] [69]. The spin state of the O₂ molecule plays a crucial role in the activated chemisorption and concurrent dissociation.

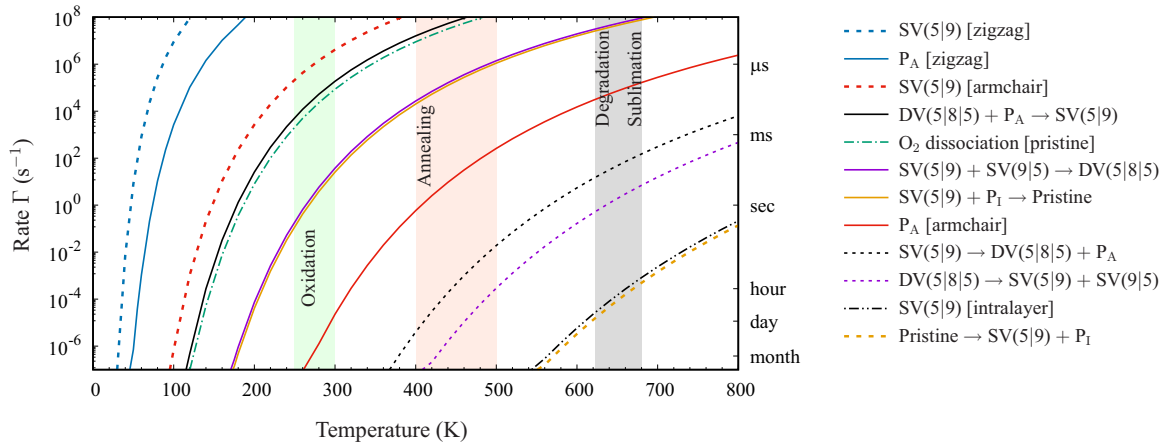


FIG. 7. Arrhenius rate Γ calculated for the various microscopic mechanisms leading to oxidation, annealing, degradation and sublimation. A typical prefactor of 10^{13} s^{-1} is assumed. The SV(5|9) and P_A are highly itinerant even below 100 K, which triggers the competing self-healing of vacancy and itinerant SV(5|9) mergers above 450 K. The degradation is accelerated above 650 K through the emission and sublimation of P_A . The chemical degradation through oxidation of pristine SLP takes place above 250 K. The overall phase diagram is in excellent agreement with the recent experimental observations [28,34,35].

The O_2 molecule undergoes a triplet to singlet spin conversion ($S = 1 \rightarrow S = 0$) with increasing proximity to phosphorene. The chemisorption in the singlet state is an activated process with 0.48 eV barrier [Fig. 6(a)], which is in good agreement with the previous calculation [41]. In this chemisorbed state, the O_2 is still weakly bound to the SLP ($E_b = -0.18$ eV), while the O atoms are bonded to the P atoms across the armchair direction with an activated O–O bond. The ultimate dissociation of the chemisorbed O_2 requires 0.13 eV barrier, and the dissociated O atoms form strong dangling P–O bonds with -4.22 eV binding energy [Fig. 6(a)]. Comparing with the results in the literature, we conclude that the activation barrier to the dissociative adsorption strongly depends on the chemistry of the molecule [75]. While the barrier for the fluorination (0.19 eV) is comparable to that of the oxidation studied here, the hydrogenation of phosphorene requires a much higher energy barrier (2.54 eV) to overcome. The fully hydrogenated phosphorene was also found to be dynamically unstable. Further, in agreement with the earlier experimental observations [39,43], we find that the rate-limiting physisorption \rightarrow chemisorption process considerably slows down with increasing layer thickness with an much higher activation barrier of 0.71 eV on the 2L phosphorene.

It would be interesting now to investigate the O_2 dissociation in the presence of lattice defects. The physisorption at a 2.06-Å height above the SV(5|9) vacancy is still weak with -0.21 eV binding energy [Fig. 6(b)]. Similar to the pristine SLP, the spin-state of the O_2 is $S = 1$. Remarkably, we find that the entire physisorption \rightarrow chemisorption \rightarrow dissociation process is spontaneous without any activation barrier. The present results are in contrast to the previous study [48], where a 0.59-eV barrier was predicted due to the consideration of a different physisorbed state, which we find to be metastable in the present calculations. The chemisorbed structure has a significantly higher binding energy of -1.17 eV compared to the same on the pristine phosphorene due to a strong P–O bond that is accompanied by an increased puckering at the SV site [Fig. 6(b)]. Unlike the case of pristine SLP,

the dissociated O atoms embed within the lattice and results in a large gain in binding energy [69]. A similar triplet to singlet spin-conversion takes place during the chemisorption at the SV(5|9) vacancy. While the O_2 -dissociation process is similar at the SV(5|66) vacancy, the only difference is that the physisorption \rightarrow chemisorption process requires 0.53 eV activation energy. In comparison, we did not find the existence of a chemisorbed state at the DV(5|8|5), and the direct physisorption \rightarrow dissociation process proceeds with a 0.56 eV barrier [Figure 6(c)]. In all cases, it is understood that once O_2 is completely dissociated, it would be difficult to remove from the lattice due to strong P–O binding.

E. Degradation phase diagram

The defect formation energies and the kinetic pathways discussed so far (Table I) provide a comprehensive insight into the defect thermodynamics and their concurrent microscopic mechanisms leading to self-healing, oxidation, degradation, and sublimation at relevant temperatures. To understand the temperature dependence of the various microscopic mechanisms, we calculate the kinetic rate and temperature phase diagram (Fig. 7) using the Arrhenius equation $\Gamma = \nu_0 \exp(-E_a/k_B T)$. The prefactor ν_0 is the Debye frequency, which is typically 10^{13} s^{-1} .

At temperatures below 100 K, both the SV(5|9) and P_A defects are highly itinerant along the zigzag direction, while all other kinetic processes are hindered (Fig. 7). However, the anisotropic SV(5|9) diffusion in the armchair direction within measurable timescale occurs only above 150 K. In contrast, the P_A diffusion along the armchair direction of the phosphorene lattice is predicted to take place at a much higher temperature above 450 K.

Self-healing of the vacancy defects are rate-limited by the merger of SV(5|9) with P_1 , which appears above 400 K (Fig. 7), which is in agreement with the experimental observation [28]. It is important to note that in this temperature range, the itinerant SV(5|9) vacancies also merge to form

bigger vacancy defects. Thus we predict a complex interplay between the competing mechanisms leading to self-healing and extended defect formation. However, phosphorization above 400 K will anneal the vacancy defects and explains the improved device performance upon 400 K vacuum annealing [76].

Further, structural degradation will be accelerated beyond 650 K. In addition to much faster SV(5|9) mergers, the larger vacancy defects are also created from the SV(5|9) point-defects through simultaneous emissions of P_A . The generated P_{AS} concurrently form P_A -pairs via diffusion and are detached spontaneously as P_A pair from the surface. Thus, above 650 K, the rapid pairwise sublimation occurs, and the overall degradation mechanism is in agreement with the recent experimental observations [28,34,35]. We also find that below 1000 K temperature, the interlayer vacancy diffusion does not play any role in degradation in few-layer phosphorene. The chemical degradation via oxidation takes place above 250 K (Fig. 7), and after that, it is impossible to remove the dissociated O atoms from the lattice.

IV. SUMMARY

We investigate the structural and chemical degradation of phosphorene within the first-principles calculations. A cohort of microscopic mechanisms is studied to develop a degradation phase diagram. The vacancy diffusion is easily accessible below the room temperature, which leads to their merger into larger vacancy defects above 400 K. The bond-rotation mechanism of two neighboring SV(5|9) defects to form DV(5|8|5) is found to be the rate-limiting mechanism. The self-healing of vacancy via itinerant adatom absorption is also triggered at a similar temperature range. In addition to the merger of mobile vacancies, the emission of the undercoordinated P atom from the point defects also generates two-dimensional anisotropic

voids above 650 K. Such P atoms are highly itinerant and thermodynamically form P_A - P_A dimer, and further degradation proceeds through the spontaneous pairwise P_A sublimation. While the interlayer vacancy diffusion in few-layer phosphorene is mostly blocked owing to the high activation barrier, the merger of subsurface vacancies is much faster at a given temperature compared to the same at the surface. However, the degradation through P emission from the point defect and the competing self-healing through the P diffusion are understandably blocked at the subsurface level. Therefore the degradation activity including oxidation primarily occurs at the surface.

The chemical degradation that is observed in ambient condition proceeds via O_2 dissociation, which we find to be accessible at the room temperature on the pristine surface, and notably the process is spontaneous at the single-vacancy site. Further, it is impossible to remove the dissociated O atoms from the lattice, and the most desirable electronic properties of phosphorene are permanently lost. Thus the present work provides with the microscopic insights into the phosphorene degradation that will have similarities with the other puckered layered two-dimensional materials.

ACKNOWLEDGMENTS

M.K. acknowledges funding from the Department of Science and Technology through Nano Mission project SR/NM/TP-13/2016, and the Science and Engineering Research Board through EMR/2016/006458 grant. The computational facilities at the Centre for Development of Advanced Computing, Pune; and at the Inter University Accelerator Center, Delhi; and at the Center for Computational Materials Science, Institute of Materials Research, Tohoku University are greatly acknowledged.

-
- [1] H. Liu, A. T. Neal, Z. Zhu, Z. Luo, X. Xu, D. Tománek, and P. D. Ye, *ACS Nano* **8**, 4033 (2014).
 - [2] L. Li, Y. Yu, G. J. Ye, Q. Ge, X. Ou, H. Wu, D. Feng, X. H. Chen, and Y. Zhang, *Nat. Nanotechnol.* **9**, 372 (2014).
 - [3] F. Xia, H. Wang, and Y. Jia, *Nat. Commun.* **5**, 4458 (2014).
 - [4] S. Zhang, J. Yang, R. Xu, F. Wang, W. Li, M. Ghufuran, Y.-W. Zhang, Z. Yu, G. Zhang, Q. Qin, and Y. Lu, *ACS Nano* **8**, 9590 (2014).
 - [5] Z. Luo, J. Maassen, Y. Deng, Y. Du, R. P. Garrelts, M. S. Lundstrom, P. D. Ye, and X. Xu, *Nat. Commun.* **6**, 8572 (2015).
 - [6] R. Fei, A. Faghaninia, R. Soklaski, J.-A. Yan, C. Lo, and L. Yang, *Nano Lett.* **14**, 6393 (2014).
 - [7] A. S. Rodin, A. Carvalho, and A. H. Castro Neto, *Phys. Rev. Lett.* **112**, 176801 (2014).
 - [8] V. Tran, R. Soklaski, Y. Liang, and L. Yang, *Phys. Rev. B* **89**, 235319 (2014).
 - [9] S. Das, M. Demarteau, and A. Roelofs, *ACS Nano* **8**, 11730 (2014).
 - [10] X. Wang, A. M. Jones, K. L. Seyler, V. Tran, Y. Jia, H. Zhao, H. Wang, L. Yang, X. Xu, and F. Xia, *Nat. Nanotechnol.* **10**, 517 (2015).
 - [11] L. Liang, J. Wang, W. Lin, B. G. Sumpter, V. Meunier, and M. Pan, *Nano Lett.* **14**, 6400 (2014).
 - [12] X. Peng, Q. Wei, and A. Copple, *Phys. Rev. B* **90**, 085402 (2014).
 - [13] J. Yuan, S. Najmaei, Z. Zhang, J. Zhang, S. Lei, P. M. Ajayan, B. I. Yakobson, and J. Lou, *ACS Nano* **9**, 555 (2015).
 - [14] S. Muduli, P. Pandey, G. Devatha, R. Babar, M. Thripuranthaka, D. C. Kothari, M. Kabir, P. P. Pillai, and S. Ogale, *Angew. Chem. Int. Ed.* **57**, 7682 (2018).
 - [15] Q. Liu, X. Zhang, L. B. Abdalla, A. Fazzio, and A. Zunger, *Nano Lett.* **15**, 1222 (2015).
 - [16] J. Kim, S. S. Baik, S. H. Ryu, Y. Sohn, S. Park, B.-G. Park, J. Denlinger, Y. Yi, H. J. Choi, and K. S. Kim, *Science* **349**, 723 (2015).
 - [17] R. Babar and M. Kabir, *Phys. Rev. B* **97**, 045132 (2018).
 - [18] H. J. Queisser and E. E. Haller, *Science* **281**, 945 (1998).
 - [19] U. Diebold, *Surf. Sci. Rep.* **48**, 53 (2003).
 - [20] A. Janotti and C. G. Van de Walle, *Phys. Rev. B* **76**, 165202 (2007).
 - [21] S. H. Song, M.-K. Joo, M. Neumann, H. Kim, and Y. H. Lee, *Nat. Commun.* **8**, 2121 (2017).

- [22] B. Kiraly, N. Hauptmann, A. N. Rudenko, M. I. Katsnelson, and A. A. Khajetoorians, *Nano Lett.* **17**, 3607 (2017).
- [23] J. V. Riffle, C. Flynn, B. St. Laurent, C. A. Ayotte, C. A. Caputo, and S. M. Hollen, *J. Appl. Phys.* **123**, 044301 (2018).
- [24] V. Wang, Y. Kawazoe, and W. T. Geng, *Phys. Rev. B* **91**, 045433 (2015).
- [25] R. Babar and M. Kabir, *J. Phys. Chem. C* **120**, 14991 (2016).
- [26] Y. Cai, Q. Ke, G. Zhang, B. I. Yakobson, and Y.-W. Zhang, *J. Am. Chem. Soc.* **138**, 10199 (2016).
- [27] Z. Qiu, H. Fang, A. Carvalho, A. S. Rodin, Y. Liu, S. J. R. Tan, M. Telychko, P. Lv, J. Su, Y. Wang, A. H. Castro Neto, and J. Lu, *Nano Lett.* **17**, 6935 (2017).
- [28] X. Liu, J. D. Wood, K.-S. Chen, E. Cho, and M. C. Hersam, *J. Phys. Chem. Lett.* **6**, 773 (2015).
- [29] Z.-D. Sha, Q.-X. Pei, Y.-Y. Zhang, and Y.-W. Zhang, *Nanotechnology* **27**, 315704 (2016).
- [30] F. Hao and X. Chen, *J. Appl. Phys.* **120**, 165104 (2016).
- [31] Z.-D. Sha, Q.-X. Pei, Q. Wan, and Z.-S. Liu, *J. Phys. Chem. C* **121**, 4708 (2017).
- [32] S. T. Skowron, I. V. Lebedeva, A. M. Popov, and E. Bichoutskaia, *Chem. Soc. Rev.* **44**, 3143 (2015).
- [33] R. Babar and M. Kabir, *Phys. Rev. B* **98**, 075439 (2018).
- [34] S. J. Yoo, H. Kim, J.-H. Lee, and J.-G. Kim, *Nanotechnology* **29**, 065702 (2018).
- [35] M. Fortin-Deschênes, P. L. Levesque, R. Martel, and O. Moutanabbir, *J. Phys. Chem. Lett.* **7**, 1667 (2016).
- [36] T. Hu and J. Dong, *Nanotechnology* **26**, 065705 (2015).
- [37] X. Li, L. Ma, D. Wang, X. C. Zeng, X. Wu, and J. Yang, *Nanoscale* **8**, 17801 (2016).
- [38] A. Castellanos-Gomez, L. Vicarelli, E. Prada, J. O. Island, K. L. Narasimha-Acharya, S. I. Blanter, D. J. Groenendijk, M. Buscema, G. A. Steele, J. V. Alvarez, H. W. Zandbergen, J. J. Palacios, and H. S. J. van der Zant, *2D Mater.* **1**, 025001 (2014).
- [39] A. Favron, E. Gaufrès, F. Fossard, A.-L. Phaneuf-L'Heureux, N. Y.-W. Tang, P. L. Lévesque, A. Loiseau, R. Leonelli, S. Francoeur, and R. Martel, *Nat. Mater.* **14**, 826 (2015).
- [40] Y. Huang, J. Qiao, K. He, S. Bliznakov, E. Sutter, X. Chen, D. Luo, F. Meng, D. Su, J. Decker, W. Ji, R. S. Ruoff, and P. Sutter, *Chem. Mater.* **28**, 8330 (2016).
- [41] A. Ziletti, A. Carvalho, D. K. Campbell, D. F. Coker, and A. H. Castro Neto, *Phys. Rev. Lett.* **114**, 046801 (2015).
- [42] T. Zhang, Y. Wan, H. Xie, Y. Mu, P. Du, D. Wang, X. Wu, H. Ji, and L. Wan, *J. Am. Chem. Soc.* **140**, 7561 (2018).
- [43] G. Abellán, S. Wild, V. Lloret, N. Scheuschner, R. Gillen, U. Mundloch, J. Maultzsch, M. Varela, F. Hauke, and A. Hirsch, *J. Am. Chem. Soc.* **139**, 10432 (2017).
- [44] K. L. Kuntz, R. A. Wells, J. Hu, T. Yang, B. Dong, H. Guo, A. H. Woome, D. L. Druffel, A. Alabanza, D. Tománek, and S. C. Warren, *ACS Appl. Mater. Interfaces* **9**, 9126 (2017).
- [45] T. Yang, B. Dong, J. Wang, Z. Zhang, J. Guan, K. Kuntz, S. C. Warren, and D. Tománek, *Phys. Rev. B* **92**, 125412 (2015).
- [46] H. Zehua, L. Qiang, L. Bo, Z. Qionghua, X. Du, L. Zhiyang, H. Fang, W. Junyong, R. Yinjuan, G. Rui, G. Eda, W. Li, H. Cheng, W. Jinlan, and C. Wei, *Angew. Chem. Int. Ed.* **56**, 9131 (2017).
- [47] Z. Qionghua, C. Qian, T. Yilong, and W. Jinlan, *Angew. Chem. Int. Ed.* **55**, 11437 (2016).
- [48] A. A. Kistanov, Y. Cai, K. Zhou, S. V. Dmitriev, and Y.-W. Zhang, *2D Mater.* **4**, 015010 (2017).
- [49] P. E. Blöchl, *Phys. Rev. B* **50**, 17953 (1994).
- [50] G. Kresse and J. Hafner, *Phys. Rev. B* **47**, 558 (1993).
- [51] G. Kresse and J. Furthmüller, *Phys. Rev. B* **54**, 11169 (1996).
- [52] J. P. Perdew, K. Burke, and M. Ernzerhof, *Phys. Rev. Lett.* **77**, 3865 (1996).
- [53] M. Dion, H. Rydberg, E. Schröder, D. C. Langreth, and B. I. Lundqvist, *Phys. Rev. Lett.* **92**, 246401 (2004).
- [54] G. Henkelman, B. P. Uberuaga, and H. Jónsson, *J. Chem. Phys.* **113**, 9901 (2000).
- [55] P. Śpiewak and K. J. Kurzydłowski, *Phys. Rev. B* **88**, 195204 (2013).
- [56] J. R. Weber, A. Janotti, and C. G. Van de Walle, *Phys. Rev. B* **87**, 035203 (2013).
- [57] F. Liu, P. Ming, and J. Li, *Phys. Rev. B* **76**, 064120 (2007).
- [58] Q. Wei and X. Peng, *Appl. Phys. Lett.* **104**, 251915 (2014).
- [59] E. J. G. Santos, S. Riikonen, D. Sánchez-Portal, and A. Ayuela, *J. Phys. Chem. C* **116**, 7602 (2012).
- [60] E. Asari, M. Kitajima, K. G. Nakamura, and T. Kawabe, *Phys. Rev. B* **47**, 11143 (1993).
- [61] J. I. Paredes, P. Solís-Fernández, A. Martínez-Alonso, and J. M. D. Tascón, *J. Phys. Chem. C* **113**, 10249 (2009).
- [62] Y. Guo and J. Robertson, *Sci. Rep.* **5**, 14165 (2015).
- [63] J. Carrasco, N. Lopez, F. Illas, and H.-J. Freund, *J. Chem. Phys.* **125**, 074711 (2006).
- [64] H. Cheng and A. Selloni, *Phys. Rev. B* **79**, 092101 (2009).
- [65] M. Kabir and K. J. Van Vliet, *J. Phys. Chem. C* **120**, 1989 (2016).
- [66] R. H. Telling, C. P. Ewels, A. A. El-Barbary, and M. I. Heggie, *Nat. Mater.* **2**, 333 (2003).
- [67] T. Trevethan, C. D. Latham, M. I. Heggie, M. J. Rayson, and P. R. Briddon, *Phys. Rev. B* **90**, 174108 (2014).
- [68] L. Liu, J. Gao, X. Zhang, T. Yan, and F. Ding, *Nanoscale* **6**, 5729 (2014).
- [69] See Supplemental Material at <http://link.aps.org/supplemental/10.1103/PhysRevMaterials.3.074008> for information on the SV(519) mergers, P_A structures, and the details for O₂ dissociation.
- [70] G.-D. Lee, C. Z. Wang, E. Yoon, N.-M. Hwang, D.-Y. Kim, and K. M. Ho, *Phys. Rev. Lett.* **95**, 205501 (2005).
- [71] L. Wu, T. Hou, Y. Li, K. S. Chan, and S.-T. Lee, *J. Phys. Chem. C* **117**, 17066 (2013).
- [72] A. Kumar, F. Telesio, S. Forti, A. Al-Temimy, C. Coletti, M. Serrano-Ruiz, M. Caporali, M. Peruzzini, F. Beltram, and S. Heun, *2D Mater.* **6**, 015005 (2018).
- [73] A. Hashimoto, K. Suenaga, A. Gloter, K. Urita, and S. Iijima, *Nature (London)* **430**, 870 (2004).
- [74] M. T. Lusk and L. D. Carr, *Phys. Rev. Lett.* **100**, 175503 (2008).
- [75] D. W. Boukhvalov, A. N. Rudenko, D. A. Prishchenko, V. G. Mazurenko, and M. I. Katsnelson, *Phys. Chem. Chem. Phys.* **17**, 15209 (2015).
- [76] L. Li, M. Engel, D. B. Farmer, S.-J. Han, and H.-S. P. Wong, *ACS Nano* **10**, 4672 (2016).